The effect of small perturbation on dynamics of absorptive LiBr-water solution

PF. Arroiabe,[1] M. Martinez-Agirre,[1] A. Nepomnyashchy,[2] M. M. Bou-Ali,[1] and V. Shevtsova[1,3]
[1)]*Fluid Mechanics Group, Faculty of Engineering, Mondragon University, 20500 Mondragon, Spain*
[2)]*2Department of Mathematics, Technion–Israel Institute of Technology, 32000 Haifa, Israel*
[3)]*IKERBASQUE, Basque Foundation for Science, Plaza Euskadi 5, 48009 Bilbao, Spain*

(*Electronic mail: x.vshevtsova@mondragon.edu)

(Dated: 25 January 2024)

In a binary solution of lithium bromide-water, even a small disturbance in the initial homogeneous mass fraction at the absorbing interface has profound effects on the entire system dynamics. This perturbation of absorption disrupts the equilibrium, leading to the formation of surface tension gradients and subsequently, Marangoni flows. While these flows are relatively weak, they result in a non-uniform distribution of density within the bulk, initiating buoyant convection. We investigate complexities of the Marangoni, solutal and buoyant convection caused by localized disruptions in uniform absorption, all in the absence of any surfactants. We have conducted numerical simulations to explore fluid dynamics and heat and mass transfer, revealing three different regimes. Initially, shortly after disturbance, variations in mass fraction and flow within the cell are primarily governed by the Marangoni force. After a finite period, the emergence of buoyant convection leads to the strong growth of velocity and significant changes in temperature and mass fraction. Finally, the destabilization of the boundary layer becomes so significant that the emission of plumes is observed. At later times, the parallel existence of two types of patterns takes on a spatially fixed form. The central part, occupied by bands (visible on space-time maps), exhibits minimal changes in time, while a periodic structure is established near the wall. This behavior can be characterized as a relaxation-oscillation mode of instability.

I. INTRODUCTION

Absorption technology can play a vital role in solving global warming problems. Among all the components of absorption machines, the absorber stands out as the main factor contributing to the reduction of heat and mass transfer[1]. The need to improve heat and mass transfer in the liquid phase of absorbers continues to attract considerable attention, as evidenced by recent reviews[2,3]. They have presented the most important experimental works dealing with the enhancement of the vapour absorption process. On theoretical aspects, significant contribution in this field has been made by Nakoryakov's team. Over nearly four decades, the team has been developing diverse models and analytical solutions, starting with the pioneering work of Grigorieva and Nakoryakov[4]. Some of the approximations introduced by them continue to be widely adopted in current practices.

Since the 1990s, the concept of using Marangoni convection to enhance heat and mass transfer on an absorbing interface has become widespread. Marangoni convection is a flow driven by surface-tension gradients, which result from interfacial inhomogeneities in either temperature or solute concentration. To highlight the influence of Marangoni convection in absorption problems, various soluble as well as dissolved in gas-phase surfactants were used in experiments and numerical simulations. The addition of a surfactant to the absorbing interface locally induces solutal convection, further accompanied by thermal and buoyant convection. Solutal Marangoni convection is an intricate phenomenon exhibiting complex and unsteady flow patterns, as discussed in the overview by Schwarzenberger et al.[5]. The interplay of solutal, thermal, and buoyant convection in the presence of absorption adds further complexity[6].

To investigate the influence of convection, numerous experimental studies have been conducted in small-scale stagnant pools[7–13]. These studies aimed to analyze how various surfactants (n-octanol, n-decanol, 2-ethyl-1-hexanol) affect water vapour absorption in the LiBr-H_2O binary mixture. Numerical approach is one of the more practical ways to study local complex heat and mass transfer phenomena in absorption[14], as well as the Marangoni convection[15–17]. In numerical simulations on absorption[7,8,18–20], the inclusion of surfactants was modeled using increased surface tension gradients correspondingly.

The conventional solution used in an absorber is the binary mixture of LiBr-H_2O. The temperature and concentration dependence of the surface tension of the mixture exhibits similarities, implying the existence of solutal and thermal Marangoni convection. However, the opposite signs of the gradients suggest the potential that these two mechanisms may counteract or even cancel each other. In order to make the convection effect more pronounced, all the simulations with realistic parameters of the LiBr-water solution were carried out using surfactants and modifying accordingly the value of the surface tension gradient with mass fraction. A more in-depth examination of surfactants can significantly complicate the problem, either by requiring the inclusion of an additional equation in the numerical approach[21] or by leading to the formation of a ternary mixture with complex cross-effects[22].

In the 1990s, there was a strong debate on numerical models concerning the initiation of Marangoni convection. The key question was whether the surfactant applied to the interface should adopt a non-dissolved drop-wise ('island' in that discussion) shape. Rie and Kashiwagi[7,19] initiated convection by

placing a surfactant (n-octanol) of an 'island' shape in several points at the interface. The enhancement of the transport phenomena due to Marangoni convection was quantified using the Nusselt and Sherwood numbers. Hozawa et al.[18] conducted simulations and experiments, adding n-octanol and n-decanol as surfactants in the center of the cavity. They provided a qualitative comparison and concluded that violent Marangoni convection persisted for an extended period, but the requirement of an 'island' shape for the perturbation was excessive. In a later work, Daiguji et al.[8] made a comparison between their numerical and experimental results of absorption in a stagnant pool using 1-octanol and 2-ethyl-1-hexanol as surfactants. However, the numerical and experimental results did not agree well. Later, Castro et al.[20] built a two-phase numerical model considering liquid and vapour phases. Even if there were still discrepancies, the agreement with Daiguji's experiments was better than the previous attempts of comparison. Then for a decade, a pause in simulating convection in stagnant pools with an absorbing interface was noted. A recent work[23] focused on a numerical method and presented a parametric study of Marangoni convection in a square with a fully or partially open top for the liquid with Prandtl number Pr=5, although for the LiBr-H_2O mixture $Pr \sim 20$.

All the efforts have collectively contributed to the understanding of the Marangoni convection influence. The overall conclusion is that the existing research recognized the critical role played by the Marangoni convection, but there is still uncertainty about the physical background. The present paper attempts to fill this knowledge gap by undertaking a detailed investigation not only the nuances of Marangoni convection but also to examine the role of gravity, which was overlooked in the previous analyses. Taking into account previous publications that raised doubts about the existence of Marangoni flow in the LiBr-H_2O mixture in the absence of surfactants, our study specifically investigates this case without additives or surfactants. Furthermore, recent experimental work[24] has focused on thermocapillary flow in this mixture without the presence of surfactants providing an opportunity for comparison.

Here, we investigate the convective instability in a LiBr-water binary mixture through numerical simulations, triggered by a local perturbation of uniform absorption. The decrease in mass fraction initiates solutal convection, leading to a local temperature change that, in turn, induces thermal Marangoni convection. At later times, we observe the development of buoyant convection. Our attention is focused towards understanding the structure of the resulting flow patterns, arising from the intricate interplay of these effects. The paper is organized as follows. The mathematical model with appropriate boundary conditions is formulated in Sec. II. Section III provides details on the numerical approach. Section IV is dedicated to model validation, presenting conventional characteristics for uniform absorption. The core of the paper is Sec. V, where we thoroughly examine flow patterns and arising instabilities. Concluding remarks are presented in Sec. VI.

II. PROBLEM FORMULATION

A. Model description

The LiBr-H_2O mixture is confined in a cavity of length L and height h, as shown in the sketch in Fig. 1. In the initial state, the mixture at a given mass fraction w_0 and temperature T_0 is motionless and water vapour occupies the space above the liquid interface. The entire system is initially in a non-equilibrium state, characterized by a temperature and mass fraction disparity between the vapour and liquid phases. The temperature of the vapour is higher than that of the liquid. As the process initiates, the water vapour undergoes absorption at the interface. As a result, the mass fraction in LiBr (w) on the interface decreases. Simultaneously, the heat released during the absorption process causes an increase in the temperature of the interface. The problem is considered under the following assumptions:

• The interface is ideally flat and without surface waves, corresponding to the limit of large surface tension.

• The absorbed mass is small compared to the mass flux of the solution. Correspondingly, the layer thickness remains constant and the velocity field in the pool is not affected by the interface displacement.

• The binary LiBr-H_2O mixture is a Newtonian fluid where the absorbent (LiBr) is non-volatile (vanishing vapour pressure). Hence, the gas phase does not contain absorbent (only water vapour).

• vapour-pressure equilibrium at the free surface is imposed.

• All the thermophysical properties are evaluated at a reference state of the mixture (P_0, T_0, w_0) and they are assumed to be constant.

In the case of a local perturbation of the mixture composition at the interface, a mass fraction gradient arises along the interface, which also causes a temperature gradient. The surface tension σ of a liquid is a composition and temperature-dependent function defined as:

$$\sigma = \sigma_0 + \sigma_T(T - T_0) + \sigma_w(w - w_0), \tag{1}$$

where $\sigma_T = (\partial\sigma/\partial T)_{w_0}$ and $\sigma_w = (\partial\sigma/\partial w)_{T_0}$ are the thermal and solutal surface tension gradients, respectively. The temperature and composition gradients give rise to surface tension gradients at a liquid/vapour interface. These gradients, in turn, induce a soluto- and thermocapillary flow in the liquid, extending to the surrounding vapour, even though the latter is not considered.

B. Governing equations

Under assumptions written in the previous section, the problem of absorption is described by the Navier–Stokes,

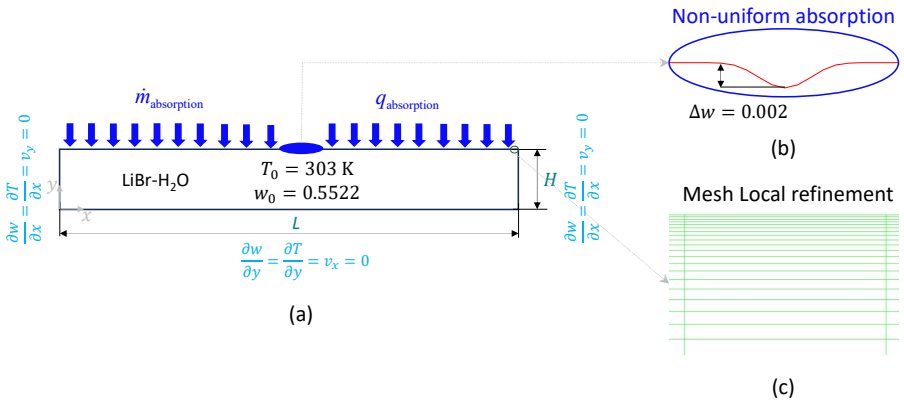

FIG. 1. (a) Sketch of the problem and boundary conditions of the model ($L = 7.5 \cdot 10^{-2}$ m, $h = 1.0 \cdot 10^{-2}$ m); (b) Local mass fraction perturbation applied in the case of non- uniform absorption; (c) Mesh refinement near the interface.

heat, and mass transfer equations:

$$\text{div}\,\mathbf{v} = 0 \tag{2}$$

$$\frac{\partial \mathbf{v}}{\partial t} + \mathbf{v}\cdot\nabla\mathbf{v} = -\frac{1}{\rho_0}\nabla P + \nu\Delta\mathbf{v} - \mathbf{g}[(\beta_T(T-T_0) + \beta_w(w-w_0)] \tag{3}$$

$$\frac{\partial T}{\partial t} + \mathbf{v}\cdot\nabla T = \frac{k}{\rho_0 c_p}\nabla T \tag{4}$$

$$\frac{\partial w}{\partial t} + \mathbf{v}\cdot\nabla w = -\frac{1}{\rho_0}\nabla\mathbf{J} \tag{5}$$

here $\mathbf{J} = -\rho_0 D\nabla w$ is the mass flux, $\mathbf{v} = [V_x, V_y]$, P, T, are the velocity, the pressure and the temperature, t is the time, $\mathbf{g}$ is the gravity. The thermal β_T and solutal β_w expansions are defined as $\beta_T = -\rho_0^{-1}\partial\rho/\partial T$, $\beta_w = \rho_0^{-1}\partial\rho/\partial w$.

The aspect ratio, defined as length to height, is kept constant, $\Gamma = L/h = 7.5$, $L = 75$ mm and $h = 10$ mm. The thermophysical properties of the lithium bromide mixture, a high Prandtl liquid $Pr = 19$, are listed in Table 1.

C. Boundary conditions

Interface:

a) vapour pressure equilibrium is assumed at the free surface, which means that the vapour pressure of water (H_2O) in the liquid phase is equal to the pressure of water vapour in the gas phase at the free surface. Furthermore, the interfacial equilibrium mass fraction w_e is assumed to be the function of temperature $w_e = f(T)$ and can be formally written as the first-order Taylor-series. In a linear approximation, it has the form of Henry's law:

$$w_e(T, P_0) = w^*_{e0} + w^*_T(T - T_0) \tag{6}$$

where w^*_{e0} is the equilibrium concentration at the reference state, and $w^*_T = \partial w/\partial T$ is the linear concentration coefficient, both depend on pressure. The validity of the linear relation was checked for two common absorbents, LiBr-H_2O and LiCl–H_2O, and found to work well under the above limitations for a wide range of temperatures and concentrations[25,26]. Commonly, in numerical simulations the relation (6) is used in the inverse form as $T_e = f(w_e)$

$$T_e = A_1 + A_2 w_e \tag{7}$$

The value of the coefficients A_1 and A_2 are given in Table I (last line).

b) vapour-liquid equilibrium in presence of absorption leads to the coupling of the heat and mass fluxes (H_{abs} is the heat of absorption, m_{abs} is the absorbed mass flux)

$$k\frac{\partial T}{\partial y} = m_{abs}H_{abs}, \tag{8}$$

$$(a)\; m_{abs} = -\frac{\rho D}{w}\frac{\partial w}{\partial y} \quad \text{or} \quad (b)\; m_{abs} = -\rho D\frac{\partial w}{\partial y}$$

Equation (8) shows that the mass flux m_{abs} can be defined in two different ways. The condition (8a), so-called 1D diffusion, considers that the penetration of the absorbate changes the volume of the solution, so the flat upper boundary begins to move[27,28]. When using condition (8b), the interface motion is disregarded.

c) In this study we use boundary condition (8a) assuming that the characteristic time of the interface motion is much larger than the hydrodynamic timescale. The interface deformation is not considered, then $V_n = 0$. This assumption was also used in previous simulations by different authors[8,20,23].

d) Balance between viscous and capillary forces is imposed

in the presence of Marangoni convection

$$\mu \frac{\partial V_x}{\partial y} = \sigma_T \frac{\partial T}{\partial x} + \sigma_w \frac{\partial w}{\partial x} \tag{9}$$

e) The remaining boundary conditions are as follows (here the subscripts n refer to the normal component):
- No-slip condition for velocity along the lateral and bottom walls $\mathbf{v} = 0$.
- Adiabatic conditions on the lateral and bottom walls $\partial T/\partial n = 0$.
- The lateral and bottom walls are impermeable $\partial w/\partial n = 0$.

Even though the problem is solved in dimensional variables, for comparison with other works, it is useful to introduce the thermal (Ma_T) and solutal (Ma_s) Marangoni numbers, which quantify the strength of the flow, as well as the Lewis number (Le), which defines the ratio of thermal to mass diffusivity

$$Ma_s = \frac{|\sigma_w| h^* \Delta w}{\mu D}, \quad Ma_T = \frac{|\sigma_T| h^* \Delta T}{\mu \alpha}, \quad Le = \frac{\alpha}{D} \tag{10}$$

here h^* is the characteristic length scale associated with the interface where the gradients occur. In simulations the physical properties are taken from[8] and all the physical quantities are given in Table I.

Initial conditions: The pool of LiBr-water at $t = 0$ is kept at $T_0 = 303\,\mathrm{K}$ and its mass fraction is $w_0 = 0.5522\,\mathrm{kg/kg}$. These initial conditions are far from the equilibrium conditions determined by the equilibrium linear function, Eq. (7). The equilibrium condition at $P = 2.3\,\mathrm{kPa}$ corresponds to $w_e = 0.4143\,\mathrm{kg/kg}$ and $T_e = 323.11\,\mathrm{K}$, respectively. The liquid at the interface reaches thermodynamic equilibrium with the vapour immediately upon contact at $t = 0$, but it takes time for the effect to diffuse into the bulk liquid. Since we consider one-phase problem, at the initial time we impose at the interface $T(t = 0) = T_e$, and $w(t = 0) = w_e$.

Flow perturbation:
Here we examine two types of vapour absorption: uniform and affected by local perturbation. In the second case, there is a disturbance in mass fraction at the interface, giving rise to Marangoni flows. It is important to note that this composition perturbation is imposed 10 seconds after the absorption process commences, with an instantaneous and singular effect. Within the localized perturbed region, the mass fraction distribution is modeled as a cosine function:

$$w = w_{0,in} - \frac{\Delta w}{4}\left[1 - \cos\left(\frac{1000\pi}{3}x + \frac{\pi}{2}\right)\right]^2 \tag{11}$$

$$34.5\ \mathrm{mm} \le x \le 40.5\ \mathrm{mm}.$$

Correspondingly, $w_{0,in}$ is the mass fraction on the interface at $t = 10\,\mathrm{s}$. A local perturbation of concentration in middle with a radius of $R_0 = 3\,\mathrm{mm}$ with max value $\Delta w = 0.002\,\mathrm{kg/kg}$ leads to a subsequent decrease in the equilibrium temperature.

We chose the squared cosine function for analyzing localized perturbations for following reasons. The difference between cosine and its square lies in the width of the peak, which is narrow in the case of squared cosine. We assume that the perturbation of absorption is strong locally. In addition, its smooth edge profile of the squared cosine helps mitigate potential numerical instability.

TABLE I. Physical properties of the LiBr-water mixture with content of LiBr in mass fractions w_0=0.5522 ($\mathrm{kg\,kg^{-1}}$) at T_0 = 303 K. All data are taken from ref.[8]. The Prandtl number $Pr = \nu/\alpha = 19$.

Diffusion	D [$\mathrm{m^2/s}$]	$1.430 \cdot 10^{-9}$
Thermal diffusivity	α [$\mathrm{m^2/s}$]	$1.235 \cdot 10^{-7}$
Thermal conductivity	k [W/m K]	$4.38 \cdot 10^{-1}$
Latent heat	H [J/kg]	$2.568 \cdot 10^{6}$
Thermal expansion	β_T [1/K]	$3.645 \cdot 10^{-4}$
Solutal expansion	β_w [1/wt%]	$-1.109 \cdot 10^{-2}$
Dynamic viscosity	μ [kg/m s]	$3.830 \cdot 10^{-3}$
Kinematic viscosity	ν [$\mathrm{m^2/s}$]	$2.358 \cdot 10^{-6}$
Density	ρ [$\mathrm{kg/m^3}$]	$1.624 \cdot 10^{3}$
Gravity	g [$\mathrm{m/s^2}$]	9.8
Surface tension	σ [N/m]	$6.00 \cdot 10^{-2}$
$\sigma_w = (\partial\sigma/\partial w)$	[N/m wt]	$1.61 \cdot 10^{-2}$
$\sigma_T = (\partial\sigma/\partial T)$	[N/m K]	$-2.1 \cdot 10^{-4}$
Equilibrium condition:	$T_e = A_1 + A_2 w_e = 242.6 + 145.8 \cdot w_e$	

III. NUMERICAL APPROACH

Governing equations (2)-(5) with boundary conditions (6)-(9) are solved in dimensional variables using the commercial software ANSYS Fluent 23.1 based on the Finite Volume Method. For this purpose, the SIMPLE scheme for pressure velocity coupling is used. Second order for pressure discretization and second order upwind for energy, momentum and species transport discretization are employed. Moreover, gradients are evaluated using Green-Gauss Node Based scheme.

A. Mesh choice and regularization

Despite its apparent simplicity, this problem inherently intertwines two different processes occurring on different time scales: slow diffusion of absorbed matter and fast Marangoni convection. This disparity in time scales complicates the numerical code and requires a sophisticated computational mesh and accurate selection of a time step. A non-uniform grid chosen for a space discretization is shown in Fig. 1. This mesh is refined near the interface to capture the interfacial heat and mass transfer phenomena and the Marangoni convection.

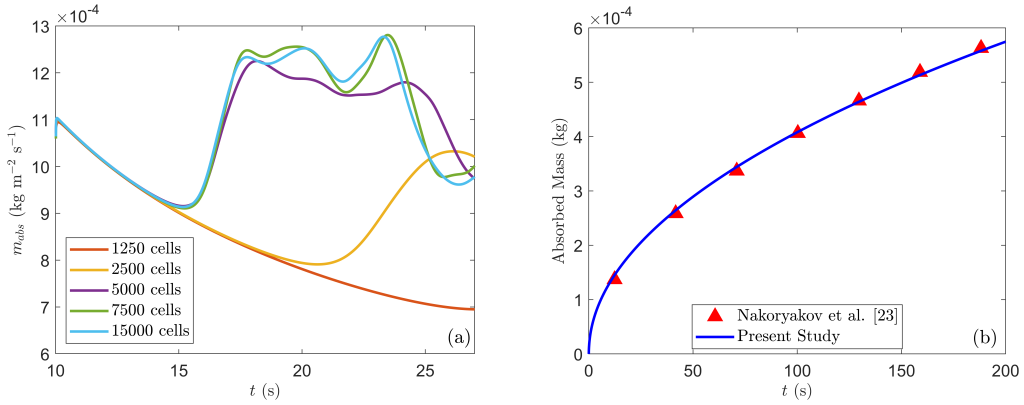

FIG. 2. (a) The mesh independence analysis using an example of the transient evolution of the average absorbed vapour mass flux in the case of perturbed absorption. (b) Comparison of our numerical results with the analytical solution obtained by[27] for the uniform vapour absorption model.

In addition, a regularization of boundary condition was used to prevent corner singularities in the system characterized by high Marangoni numbers. The cosine regularization equation for corner regions proposed by Wanschura et al.[29] helps to smooth out these effects, leading to a more accurate and stable representation of Marangoni convection dynamics. The surface tension gradients near the cell ends are transformed as:

$$\sigma_{T,w} = \sigma_{T,w}\left[1-\frac{1}{4}\left(1-\cos\left(200\pi x+\pi\right)\right)^2\right] \quad x \leq 5 \text{ mm} \tag{12a}$$

$$\sigma_{T,w} = \sigma_{T,w}\left[1-\frac{1}{4}\left(1-\cos\left(200\pi x\right)\right)^2\right] \quad x \geq 70 \text{ mm} \tag{12b}$$

The regularization of boundary conditions serves two distinct purposes. First, it plays a crucial role in preventing the formation of artificial/spurious vortices at the triple points at initial times. Second, it helps mitigate what is known "cold corner problem"[30] even though there is no external temperature gradient. Over time, the mass fraction gradient near the walls become significant, as does the temperature gradient due to the equilibrium condition, see Eq. (7). Note, the Prandtl number of the LiBr-water mixture is high, $Pr = 19$. The gradients of the mass fraction near the side walls can be seen in Fig.10(b).

B. Mesh independence analysis and model validation.

In the case of perturbed absorption, strong Marangoni convection occurs. Comparing with the uniform absorption case, this case is more challenging to calculate. Thus, the perturbed absorption case was selected to study the mesh independence and five different grid configurations of 1250, 2500, 5000, 7500 and 15000 cells were considered, which have the varying number of cells in both x and y directions.

Figure 2(a) compares the change in the average mass flux of absorbed vapour at the interface over time at different meshes. One of the objectives of this study is to investigate the effect of Marangoni convection, so the comparison was focused on the time window 10 s $\leq t \leq$ 27 s. Comparison of different grids is especially important during this period of time, characterized by strong development of flow field that precede the establishment of an instability (see more details in Section V). Within this time interval, the differences in results from the coarsest to the finest mesh, relative to the 15000-cell mesh are 22.4 %, 16.1 %, 0.6 % and 0.2 %, respectively. Although both 5000 and 7500 cells grid achieve similar quantitative results, the second one follows better the transient profile of the thinnest grid. Thus, to have a good compromise between a reduced computational cost and numerical accuracy, a grid of 7500 cells with an average aspect ratio of 19 was chosen.

To validate the model, the results are compared with the analytical solution proposed by Nakoryakov et al.[27]. The comparison of curve and symbols in Fig. 2(b) shows a close similarity in absorbed mass fluxes, indicating that our model accurately reproduces the analytical solution. For further validation, quite often, numerical results are compared with experiments by Daiguji[8]. However, in absorption experiments the error bar is quite large, and this issue worsens in the case of weak absorption when no surfactants are added. Nevertheless in section V A, a comparison of our results with recent experiment[24] reveals a very good agreement. Once the model is validated, we proceed to examine the transient behaviour of the absorption process.

For the sake of generality, the results below will be presented using dimensionless cell length, $0 < x/L < 1.0$, for the horizontal dimension and $0 < y/h < 1$ for the height, even though the calculations were performed in a dimensional

form. It is worth noting that all the observations exhibit symmetry relative to the center of the cell. Consequently, the majority of the figures below will only be depicted in the right half of the cell, i.e., $0.5 < x/L < 1.0$. These changes aim to make the description more concise while maintaining its technical precision.

IV. RESULTS. UNIFORM ABSORPTION OVER THE INTERFACE

In this section, we consider a homogeneous absorption without thermal or solutal perturbations. This system is always stable from the viewpoint of buoyant effect because the solution density decreases with height. Consequently, convective flow is absent, and therefore, absorption is governed by diffusion process.

Figure 3 illustrates the time-dependence of two key quantities: the absorption mass flux (panel a) and the mass fraction (panel b). As a result of disparities between initial and equilibrium conditions, both absorption mass flux and LiBr mass fraction undergo abrupt changes at the beginning. The long-term behavior is shown in the main graphs, where the curves nearly align with the axes. After a while, these gradients decline considerably. To illustrate a more detailed view of the temporal dynamics, the insets show these quantities on a shorter time scale.

In our model, taking convection into account, perturbations to the LiBr-H_2O mixture are introduced at $t = 10$ s. This specific time point is depicted by vertical dotted lines in Fig. 3. Note that the heat and mass transfer patterns at this moment will serve as the initial conditions for a problem involving the presence of Marangoni flows. The mass fraction and temperature patterns at $t = 10$ s are shown in Fig. 4. Gradients in temperature and composition develop on different scales because of the substantial difference between thermal and molecular diffusivities. Consequently, the thermal boundary layer develops much faster than that of the mass fraction. This difference can be quantified by a large Lewis number, $Le = \alpha/D \sim 90$. During the first ten seconds, the changes of temperature and concentration fields caused by the thermal and mass diffusion do not reach the cell bottom.

V. DYNAMIC CHANGES IN ABSORPTION IN THE LIBR-WATER BINARY MIXTURE: INSTANT PERTURBATION RESULTS

We consider a minor disturbance of the mass fraction on the absorbing interface as given in Eq. (11), which results in the formation of a localized area with a lower LiBr mass fraction. The interplay between the main liquid pool and this region of decreased concentration leads to complex and rich dynamics. This complexity arises due to the emergence of a surface tension gradient, which induces the so-called solutal Marangoni convection. Due to the equilibrium condition on the interface, the decrease of mass fraction leads to a local change in the temperature, which in turn, triggers the thermal Marangoni convection. We detail three regime of flow dynamics.

A. Marangoni dominant flow, $t < \tau_1$.

The core of convection is the lowered mass fraction of the LiBr-water mixture in the disturbed region, corresponding to a smaller surface tension. The expectation is that Marangoni spreading should start at the edge of perturbation and move outward towards a higher surface tension. At the initial moments of convection development, we observe an intriguing phenomenon where the flow direction appears to defy our expectations. The gradients of surface tension due to temperature and composition have different signs. This implies that the forces driving solutal and thermal Marangoni convection are oriented in opposite directions. Even though the formal evaluation, according to the initial value of perturbation, provides that the solutal Marangoni number is slightly higher than the thermal one, the results show that the flow is directed towards the center of perturbations.

The velocity profile only 0.1 s after the perturbation, i.e., at $t = 10.1$ s, is negative, see the dashed curve in the left part of Fig. 5. This means that the flow is directed opposite to the expected flow direction due to solutal convection. This puzzle is related to the equilibrium condition at the interface. To evaluate the relative contributions of solutal and thermal Marangoni convection to viscous stress in Eq. (9), we will compare the capillary forces on the interface using equilibrium condition expressed by Eq. (7). It follows that $\partial T/\partial x = A_2\,\partial w/\partial x$. Then the net capillary forces can be written as

$$\sigma_T \frac{\partial T}{\partial x} + \sigma_w \frac{\partial w}{\partial x} = (A_2\,\sigma_T + \sigma_w)\,\frac{\partial w}{\partial x} \tag{13}$$

Although solutal variation of surface tension $|\sigma_w|$ is almost 30 times larger than the thermal one $|\sigma_T|$, the quantity A_2, which is on the order of a hundred, alters the balance of their contributions (see Table 1). Thus, the thermal Marangoni effects dominate and since $\sigma_T < 0$, the net flow is directed inward. It should be noted that this estimation is relatively rough, because there is a temperature rise due to the release of latent heat. However, it helps to explain the flow direction.

At the first moments of observation (dashed blue curves in Fig. 5), the Marangoni flow is localized inside two vortices of opposite signs near the interface. The vortex expands (as shown in series of snapshots), and despite the continuity that pulls up fresh solution with higher surface tension from beneath the interface, the extension of the vortex leads to a decrease in the gradients $\partial w/\partial x$ and $\partial T/\partial x$ on the surface. The damping effect of opposite signs of the gradients also contributes, resulting in a reduction in velocity. The velocity drops by almost an order of magnitude in 0.4 s, compare the blue and red curves at $t = 10.1$ s and $t = 10.5$ s. At $t = 11$ s the flow practically fades, see V_x profile shown by the gray curve.

In the region of the interface not affected by the flow, the absorption of water vapour remains in the usual mode, and the thickness of the boundary layer increases due to diffusion. This phenomenon is illustrated by parallel curves presenting mass fraction when $x/L > 0.6$. During this time, the

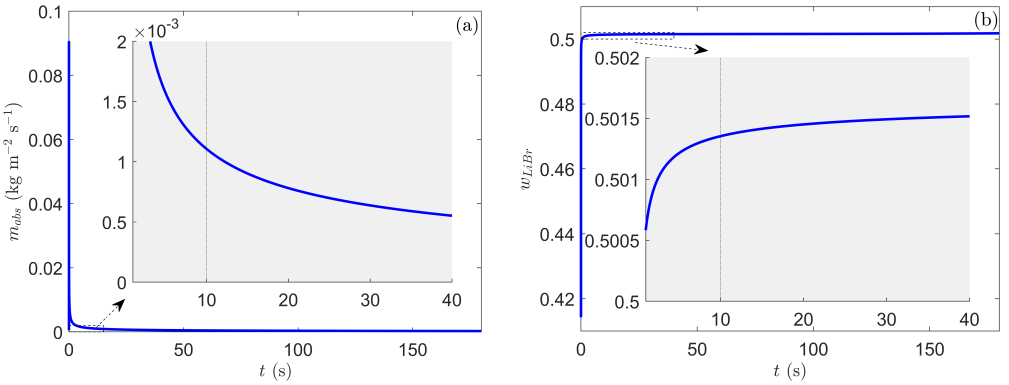

FIG. 3. Transient evolution of (a) the absorption mass flux and (b) mass fraction in diffusive regime at the interface.

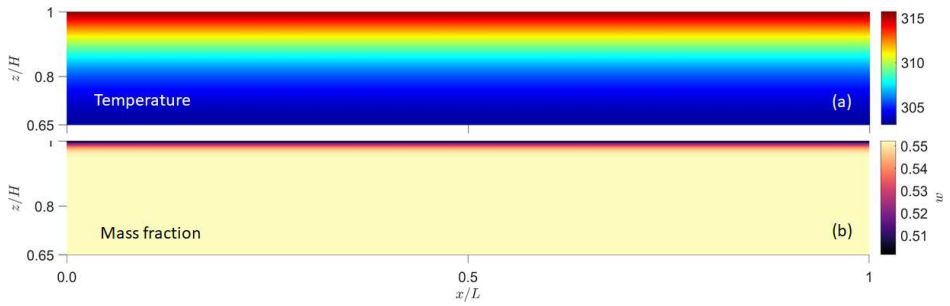

FIG. 4. LiBr mass fraction and temperature contours at $t = 10$ s. For better visibility, patterns are shown only in the upper 35% of the cell, since there are no changes at the lower part of the cell.

Marangoni vortex mixes the solution, leading to the gradual formation of a non-uniform density distribution in the x-direction beneath the initially perturbed region. Here the density variations may cause both solutal and thermal convection. Using the values in Table 1 gives the following estimate

$$Ra_T = \frac{g\beta_T \Delta T\, h^3}{\nu\alpha} \sim \frac{g\Delta\rho_T^{eff} h^3}{\nu\alpha} = 3.37 \cdot 10^7 \Delta\rho_T^{eff} \quad (14)$$

$$Ra_w = \frac{g\beta_w \Delta w\, h^3}{\nu D} \sim \frac{g\Delta\rho_w^{eff} h^3}{\nu D} = 2.91 \cdot 10^9 \Delta\rho_w^{eff} \quad (15)$$

Figure 5a shows that at $t = 11$ s the mass fraction variations are of the order of magnitude 10^{-4} and density $\sim 10^{-6}$, respectively. From Rayleigh estimations above, it follows that even these small variations will initiate predominantly solutal convection, which will be subsequently accompanied later by thermal convection. Indeed, the snapshot (d) clearly demonstrates the birth of small vortices driven by gravity. These vortices develop sweepingly and, in less than a second, reach the interface, carrying a cold and concentrated solution (as shown in snapshot (e)). Gradients $\partial w/\partial x$ and $\partial T/\partial x$ start to grow at the contact points between vortices, causing an increase in velocity, see the yellow curves in panels (a) and (b). Shortly after, at $t = 13$ s, gravity exerts local influence, resulting in a rapid increase in velocity. At the contact line between two big vortices driven by gravity and Marangoni stresses, the boundary layer of mass fraction becomes highly compressed and ultimately ruptures. This is depicted by the green curve, touching the abscissa at $x/L \sim 0.57$ (panel a). In addition, the vortex driven by gravity begins to push the vortex driven by Marangoni towards the wall.

It is intriguing that the flow direction towards the center coincides exactly with the flow direction noted by Bufetov et al.[24] in recent experiments, even though no further explanation was provided. Moreover, they stated that at the beginning of the process horizontal velocity values reach 0.8 mm/s in the direction opposite to the x-axis, after which motion in the x-axis direction becomes predominant. This completely aligns with our findings even quantitatively, see the blue and green curves in Fig. 5(b). Note that their experimental conditions were slightly different, e.g., $w_0 = 0.58$ kg/kg, $T_0 = 297.65$ K and $P_0 = 2.03$ kPa.

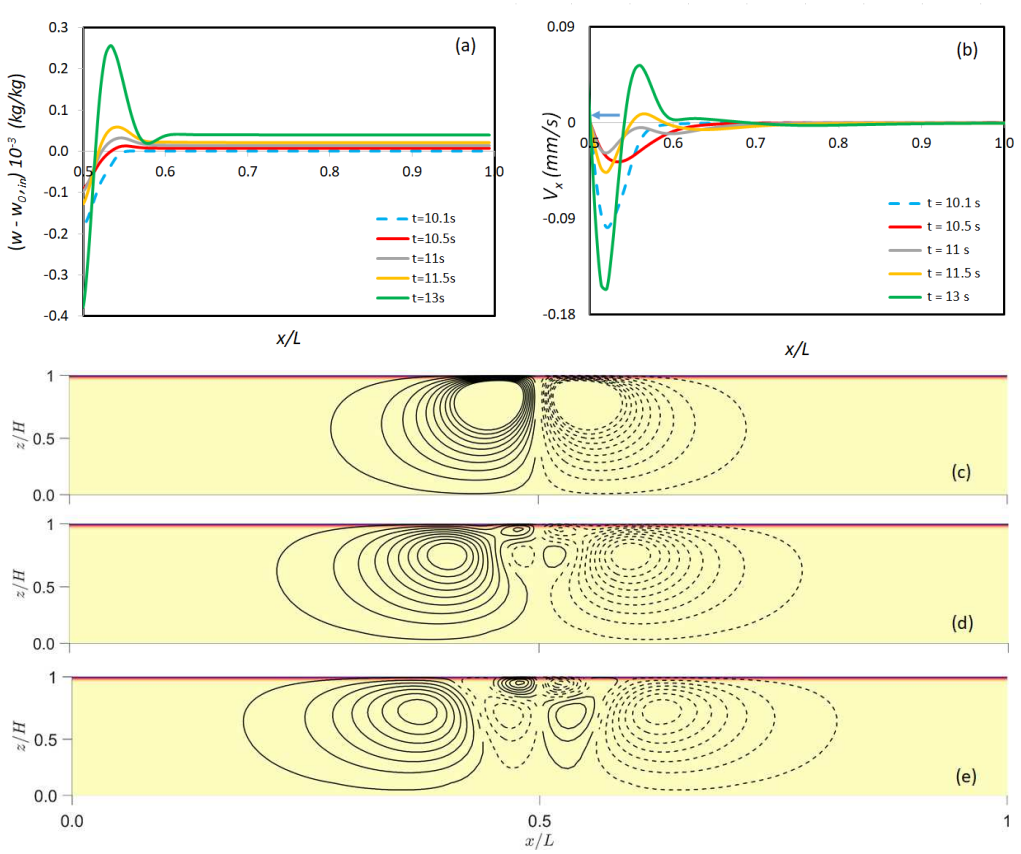

FIG. 5. *First regime*, $t < \tau_1$. Temporal evolution of (a) mass fraction ($w - w_{0,in}$) and (b) velocity V_x along the interface. Recall that $w_{0,in}$ is the mass fraction on the interface at $t = 10$ s. For better clarity, the mass fraction and velocity are shown in the half-cell. The temperature evolution is not shown because at the interface it has the same profile as mass fraction due to equilibrium. The level lines in snapshot (c) illustrate the development of the Marangoni flow at $t = 10.5$ s and in (d)-(e) detail the origin of a buoyant flow, $t = 11$ s and $t = 11.5$ s. The visibly uniform boundary layer of the mass fraction, shown in red in the snapshots, indicates that the flow on the interface has little effect on the diffusion process. Counterclockwise circulation in the vortices is shown by the dashed curves.

B. Development of instability, $\tau_1 < t < \tau_2$

This regime is characterized by strong changes in various aspects of the system dynamics, including fluid velocity, temperature distribution, and mass fraction profiles. In Fig. 6, the depicted quantities mirror those in Fig. 5 but on a scale a thousand times larger. Notably, the green curves from Fig. 5 become nearly invisible in the new scale, emphasizing a substantial increase in both mass fraction and velocity at the interface. This growth results from the rapid development of buoyant convection at high Rayleigh numbers. In addition, the growing vortex is partially driven by the Marangoni force, as evidenced by the location of the vortex center close to the interface. It should be noted that the flow undergoes a change in direction, predominantly moving from the center. Only within a small zone of the initial disturbance, the velocity maintains a negative direction, although very low.

In Fig. 6(a)-(b), the curves at successive times ($13\,s < t < 20$ s) clearly demonstrate that the flow on the interface reaches the sidewall at $t = 18$ s. The main vortex expands, its strength weakens at the periphery, creating an opportunity for the formation of a small-scale Marangoni-driven flows, see snapshot at $t = 18$ s. The flow is confined laterally, and when the elongated roll occupies all the space, the convection process is in-

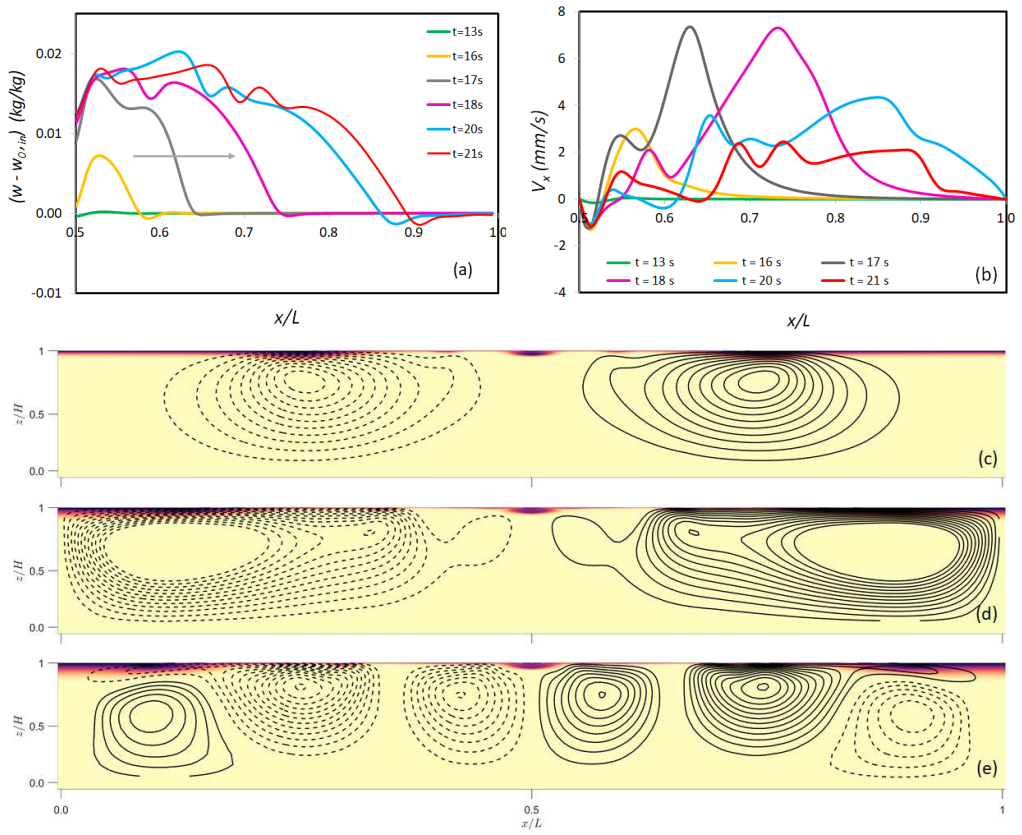

FIG. 6. *The second regime,* $\tau_1 < t < \tau_2$. Temporal evolution of (a) mass fraction $(w - w_{in})$ and (b) velocity V_x along the interface. Note that scale here for the same quantities is three order of magnitude different in comparison with Fig. 5. The general trend involves the spreading of higher mass fraction along the interface and the increase in velocity until it reaches the sidewall. The gray arrow depicts the propagation of mass fraction leading front over time. The level lines of the stream function in the snapshots at 18 s, 20 s and 21 s illustrate the growth and rupture of the flow pattern. The reddish colors corresponding to the lower mass fraction in the snapshots show that an initial boundary layer of the mass fraction is ruptured; it is retained in the central part affected by the Marangoni flow, and the remaining part is displaced towards the sidewall.

terrupted until a new pattern of convective rolls emerges with an aspect ratio close to unity, see the snapshot at $t = 21$ s. This is characterized by a strong drop in velocity, which is illustrated by comparison of the magenta and red curves in Fig. 6(b).

Simultaneously, the diffusion layer is washed off toward the sidewall, establishing an increased mass fraction at the interface. The distribution of w is non-uniform, leading to an increase in surface tension in regions with lower w content. This creates gradients that induce the emergence of new zones with local Marangoni vortices. Nevertheless, the gravity-driven vortex remains powerful in this regime, preventing the expansion of these new Marangoni vortices. Consequently, they remain pressed from below to the surface, characterized by lower mass fraction regions, serving as precursors to the formation of forthcoming plumes.

Interestingly, the large vortices block the extended region of lower mass fraction (albeit variable) near the sidewall, creating an elongated Marangoni-driven vortex in close proximity to the surface, see Fig. 6(e). This corner vortex persists throughout the entire convective process.

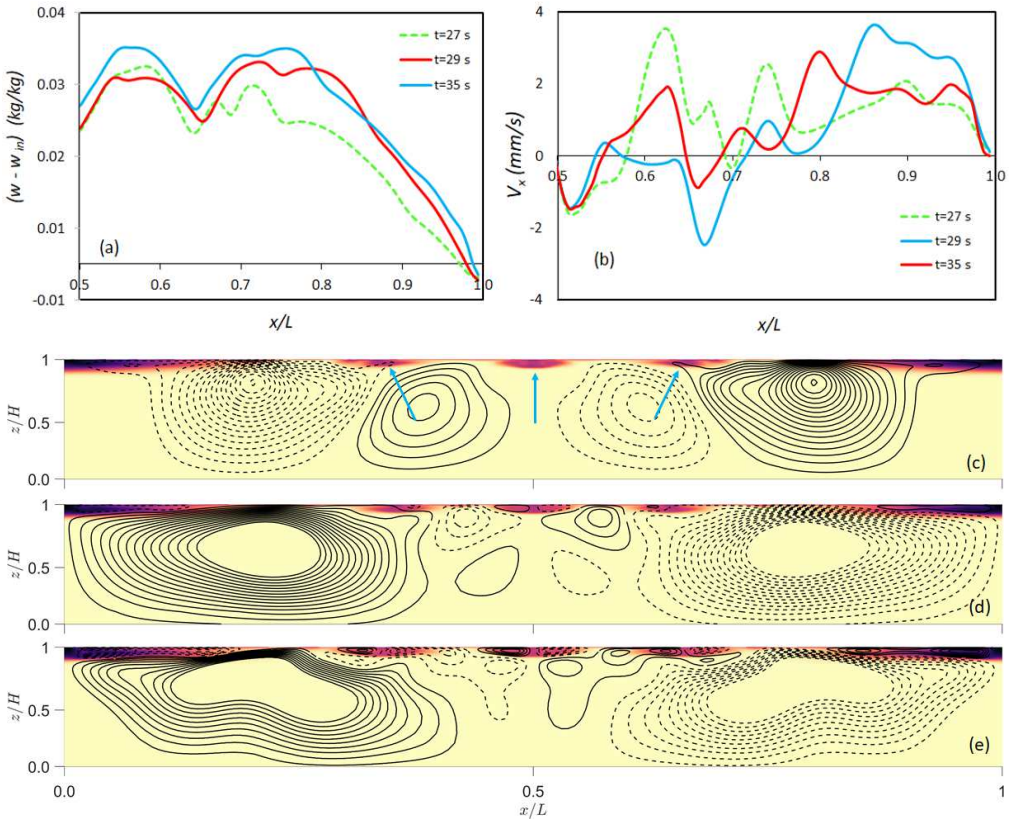

FIG. 7. *The third regime,* $t > \tau_2$. Temporal evolution of (a) mass fraction ($w - w_{in}$) and (b) velocity V_x along the interface. The general trend suggests slow temporal changes in the mass fraction profile, with still significant variations in the velocity profile. The flow does not have a predominant direction. The snapshots (c-e) corresponding to $t = 28$ s, 31 s and 37 s outline the flow periodicity and indicate that, due to strong competition, the vortices in the central part lose strength and break up into smaller ones. The reddish colors illustrate the formation of lens-like structures near the interface, as indicated by blue arrows at the upper snapshot.

C. Formation of plumes and periodic patterns, $t > \tau_2$

Starting with the formation of several approximately equal vortices ($t = 21$ s), the intensity of the gravitational flow decreases. For a given aspect ratio $\Gamma = 7.5$, the maximum number of large rolls dominated by gravity after splitting never exceeds three within a half-cell or six across the entire cell. The ongoing convective process continues, fueled by non-uniform absorption.

When the large vortex splits, the newly formed vortices create highly variable velocity along the interface. The accompanying variations in mass fraction, which are also considerable, provide the basis for a solutal Marangoni flow. Interestingly, the mass fraction profiles show less variability over time compared to the velocity profiles. A comparison of the curves of the same colors in Fig. 7(a) and Fig. 7(b) highlights this difference. The flow does not exhibit a predominant direction. Our observations are consistent with the experiments by Bufetov et al.[24] that have indicated the absence of a prevailing flow direction; instead, sporadic movements in different directions are constantly observed.

The 3rd regime is characterized by setting the time and spatial periodicity in the system. Over time, the flow pattern begins to practically repeat itself with a period of *sim*5.2 s. This repeatability is illustrated by comparing snapshots (d) and (e) in Fig. 7 where the sizable vortices with negative circulation dominate the region adjacent to the wall. Despite this pattern, the interaction between smaller vortices persists near the inter-

face. As a result, the velocities profiles on the interface are not identical (compare the red and blue curves in panel (b)), but do share similarities in the way they change values and sign. In contrast to velocity, mass fraction profiles exhibit a notable level of repeatability. Once again, comparison of the red and blue curves in panel (a) shows a high degree of similarity in how these profiles develop over time.

In regions where the mass fraction w is locally reduced, lens-like structures form. The driving force of all these structures is the soluto-thermal Marangoni shear stresses, operating on different length scales and fuelled by absorption. The snapshots in Fig. 7 reveal a somewhat ordered range of these patterns.

It is noteworthy that, unlike the typical role of Marangoni convection in promoting spreading, in our case, it results in the opposite effect. Once these lens-like cells form, they exhibit minimal horizontal growth because the flow is directed from the periphery towards the center. The rationale for this flow direction was discussed considering the initial perturbation in section V A. Furthermore, these localized cells do not exhibit visible vertical growth. On the one hand, they are pressed against the interface by large gravity rolls. The density inside "lens-like" cells is lower than below, and buoyant convection is not strong enough to replace it with a heavier solution. On the other hand, the diffusion time is significantly longer than the viscous time, and the diffusion process cannot be easily observed. A close inspection of lens-like cells reveals typical plume features, as illustrated by the density profiles in Fig. 8c.

The subsurface layer, containing lens-like cells, is dynamic because these cells move horizontally. Initially, the positions of the cells at any given time seem sporadic, as they are transported left or right by large convective rolls. The cell displacement can be traced by following them in the snapshots in Fig. 7.

The only stationary cell is situated adjacent to the wall and encloses a lower mass fraction from the initial boundary layer swept away from the rest of the interface. Its horizontal elongation depends on the number and placement of large rolls. Particularly in this region, an instability in the form of relaxation oscillations[5,31] is observed at the later times. This behavior is associated with a repeated interplay between Marangoni instability, buoyant convection, and the restoring effects of absorption.

D. Creating of ordered patterns.

1. Dynamics of mass fraction

The periodic nature of the phenomena is best illustrated by the space-time map presented in Fig. 8. The space-time maps depicted in panel (a) and (b) illustrate the evolution of mass fraction on the interface. Meanwhile, panel (c) presents the density distributions across the cavity. The map in panel (a) captures the various regimes described above, providing a coherent picture of the dynamic evolution of mass fractions. The overall visual impression suggests a pattern characterized by four distinct vertical bands, becoming clearly defined from the onset of the 3rd regime. Panel (a) offers insights into the observed trends. In the first regime, variations in mass fraction (w) can be noticed only in the central part of the cell, where Marangoni flow has emerged. The second regime evidences a significant and abrupt change in the mass fraction magnitude and spreading along the interface because buoyant convection enters into play. A subtle periodicity in space also can be noticed in this regime. However, the periodicity evident both in space and time is the distinct feature of the third regime.

To unravel the puzzle encapsulated within these bands, we took two snapshots at $t = 27.7$ s and $t = 35.5$ s detailing the mass fraction across the cell. These snapshots are superimposed onto a space-time map shown in panel (b). These snapshots clarify that the light color between the stripes corresponds to the location of the plumes. Based on the width of this light-colored region, we can further subdivide the 3rd regime into (a) and (b). The broader space between the strips in regime III(a) suggests that the plumes are undergoing horizontal movement, and the smaller plumes merge with the larger ones. As time progresses, the pattern stabilizes into regime III(b).

The birth and coalescence of small plumes are better illustrated by density profiles that incorporate both mass fraction and temperature variations. The density profiles for different regimes are depicted in Fig. 8(c) at the top of the cell at high magnification. Similar to the mass fraction, these profiles represent plumes sinking with a characteristic mushroom-shaped head. The density inside the plumes is lower than that outside, and their evolution is driven by diffusion and Marangoni stresses. These phenomena are sustained by the absorption of water vapour, contributing to the overall dynamics of the plumes.

In addition to the spatially ordered bands, the system's dynamics exhibit periodicity over time. The periodicity is observed in the space between the sidewall and the band closest to it. This can best be seen on the side of the band facing the wall, shown by red/yellow colors in Fig. 8(a).

2. Development of the velocity field and absorbed mass flux

We investigate temporal periodicity by analyzing the dynamics of the velocity field. The space-time map in Fig. 9(a) presents the evolution of axial velocity at the interface, revealing clearly defined maxima and minima. Flow dynamics further clarify the selection of regimes discussed for mass fraction. The most energetic flow field is observed during the 2nd regime, even though regime IIIa remains highly changeable.

In the second regime, there are distinct peaks of V_x at $t \sim$ 18 s, 23 s, 28 s, indicating moments when the high-velocity flow reaches the sidewalls. As a result, there is a pronounced shift in mass fraction towards the sidewall, as visually represented by the light blue color in Fig. 8(a). This observation highlights a clear alignment between the time periodicity of mass fraction (w) and the flow, revealing with a period of approximately 5.2 s.

In regime IIIa, the instability manifests as two distinct, albeit changeable, patterns occurring in different regions of the

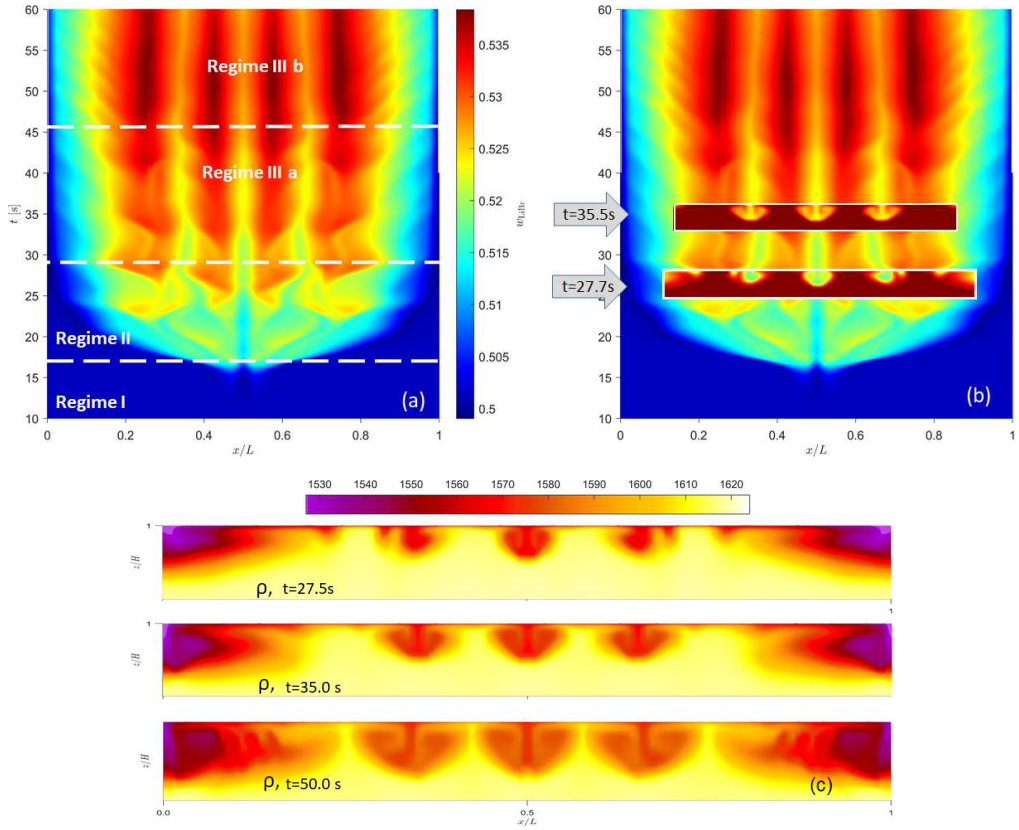

FIG. 8. (a,b) The mass fraction dynamics shown on the interface: (a) the space-time map revealing three key regimes caused by non-uniform absorption; (b) the space-time map with superimposed snapshots of w across the cavity at $t = 27.7$ s and $t = 35.5$ s illustrating the nature of the periodicity; (c) Density profiles are shown in regimes II, IIIa, and IIIb, highlighting the mushroom-shape of the plumes and their evolution over time. The figures show that, as time progresses, smaller plumes merge with larger ones. The full density $\rho(x,y)$ is shown in the top 15% of the cell. The initial density is $\rho = 1624\,\mathrm{kg/m^3}$, see the color map for scale.

container. The band features are somewhat noticeable in the central part, and simultaneously, a new periodic structure with a variable period forms near the sidewalls. The transitions, outlined by dark colors in the map, were detailed in the snapshots in Figs. 6-7, illustrating the interplay between gravity and Marangoni stresses, which leads to the merging, growth, and collapse of vortices.

In regime IIIb, the parallel existence of two types of patterns takes on a spatially fixed form. The central part, occupied by bands, exhibits minimal changes in time, while a periodic structure near the wall becomes established with a consistent period of approximately 3.9 seconds. This behavior can be characterized as a relaxation-oscillation mode of instability[5,6,31]. A noticeable change in the oscillation period occurs during the transition between regimes II and IIIb. While oscillations in regime IIIa do not show a clear period, they revived again in regime IIIb with a shorter period compared to regime II.

The space-time maps in Fig. 9 reveal a strong correlation between the absolute value of the velocity (panel a) and the absorbed mass flux (panel b). The observed connection, in part, could be attributed to equilibrium conditions at the interface, when variations in one variable are balanced by changes in the other ones. The time evolution of the absorbed mass flux clearly exhibits the absorption-limited nature of the instability, illustrating the gradual loss of energy within the bands over time.

Quantitative characteristics of the absorption mass flux are

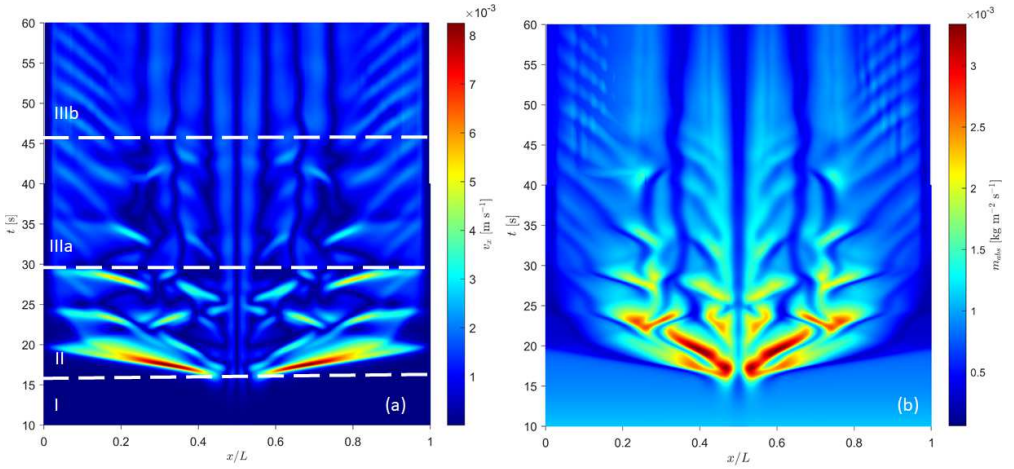

FIG. 9. The space-time maps for (a) the interface velocity (absolute value) and (b) the absorbed mass flux. For clarity of the maps, the separation between regimes is indicated only by numbers and only on the velocity map. The appearance of the maps reveals the correlation between the absolute value of the velocity and the absorbed mass flux.

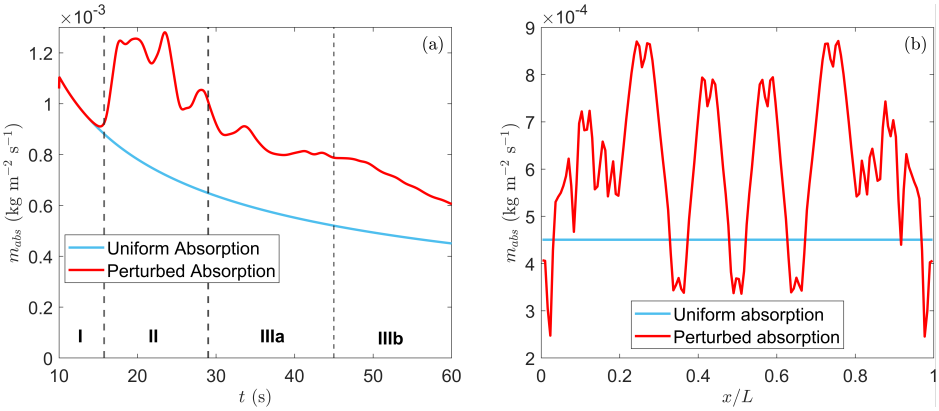

FIG. 10. (a)The comparison of time evolution mass flux in uniform regime of absorption and with perturbation. (b) Distribution of absorbed mass flux over the interface at $t = 60$ s.

given in Fig. 10. Panel (a) illustrates that the absorption mass flux sharply increases in the second regime, characterized by the rising interface velocity. Later, its dynamics follow the development and fading of the flow, asymptotically approaching the mass flux of uniform absorption. Panel (b) compares the distribution of mass flux along the interface at $t = 60$ s for uniform and perturbed absorption. Lower values of m_{abs}, representing mass flux, are observed near the wall, where the LiBr-H_2O mass fraction is smallest. It is evident that absorption efficiency is significantly higher when the mass fraction at the interface differs from the equilibrium one.

E. Bulk flow and temperature fields

The above analysis places significant emphasis on the dynamics occurring at the interface. Here we shift the focus towards bulk processes. The quantitative comparison of velocity across the cell in the second regime, at $t = 18$ s when the flow reaches the sidewall, and at the end of regime IIIb $t = 60$ s, is

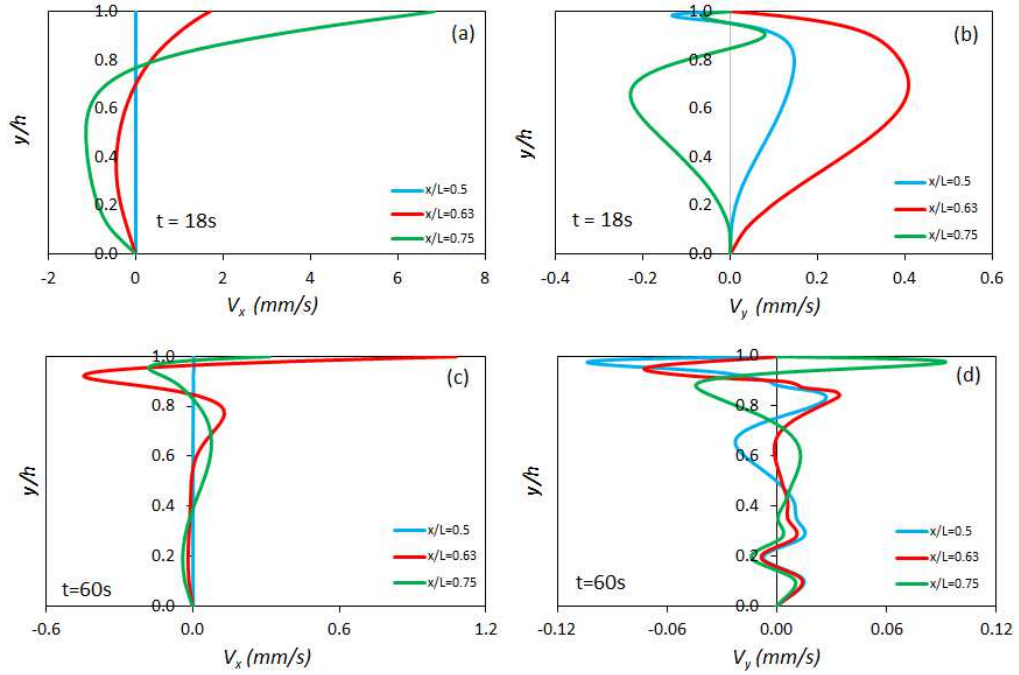

FIG. 11. Axial velocities (a-c) and vertical velocities (b-d) across the layer at different locations along the container in the second regime ($t = 18$ s) and at the end of regime IIIb ($t = 60$ s). The different colors of the curves identify the locations. The upper row represents velocities in regime II and the bottom raw at the end of regime IIIb.

shown in Fig. 11. Three key locations along the x-direction are chosen as the most illustrative: the midpoint ($x/L = 0.5$), the region of intense vortex competition ($x/L = 0.63$), and the area of the near-wall large vortex ($x/L = 0.75$).

The first observation is that, regardless of the moment in time under consideration, the magnitude of V_x surpasses that of V_y by an order of magnitude. Another observation is that at later times, $t = 60$ s, the velocity in the volume weakens significantly. Again, these observations coincide with the experimental findings by Bufetov et al.[24]. Both velocities exhibit energetic behavior only at the upper part of the cell when $y/h > 0.8$ and considerably attenuate below. This trend suggests that the buoyant force loses influence on the velocities, which was significant at $t = 18$ s. Thus, at later times the strength of the flow is controlled by water vapour absorption through Marangoni stresses.

In the above analysis, we did not show the temperature variation because, at the interface, it is similar to the mass fraction due to the equilibrium condition, the Henri law. However, the temperature and mass fraction are not the same in volume, since the thermal diffusivity and diffusion coefficient differ by a factor of 100. Figure 12 displays two patterns of the thermal field: the top snapshot shows the temperature distribution at $t = 60$ s, capturing the impact of buoyant-Marangoni convection. For the same time moment, the lower snapshot highlights the variation in thermal fields between cases where absorption occurs with convection and a purely diffusive regime. An unexpected finding is that convective instability primarily influences the thermal dynamics within the upper part of the cell. The inset highlights the observation: in the lower portion of the cell, $y/h < 0.5$, convection elevates the temperature only slightly, by about 0.5 K, despite imposing adiabatic conditions on the lower wall. Interestingly, at t=18 s, the convective flow locally reduces the temperature below the temperature created by the diffusion process. This occurrence is associated with the circulation of the flow inside the vortex beneath the surface layer.

VI. CONCLUSIONS

We have examined the absorption dynamics in the LiBr-H_2O binary mixture, considering both uniform and perturbed absorption scenarios. Uniform absorption in the LiBr-H_2O mixture, upon contact with water vapour, follows a diffusive process, with the thermal field advancing much faster than the

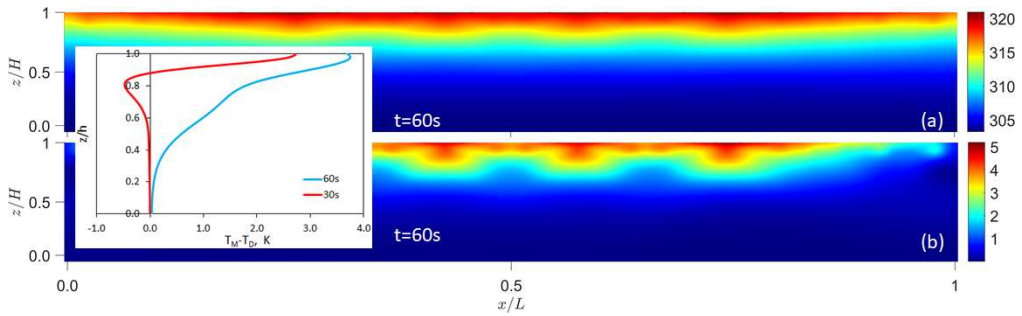

FIG. 12. The temperature field at $t = 60$ s. (a) The top snapshot depicts the temperature distribution, illustrating the influence of convection. (b) The lower snapshot shows difference in the thermal field between case with buoyant-Marangoni convection and pure diffusive regime. The inset quantifies the difference and displays it at $t = 30$ s and 60 s.

mass fraction due to the difference in thermal and mass diffusivities by two orders of magnitude.

To align with real experiments, the instant perturbation does not occur at zero time but is introduced slightly later, after 10 seconds of uniform absorption. This perturbation involves a decrease in the mass fraction of LiBr in a small area at the center. This change leads to the emergence of solutal and thermal Marangoni convection, followed by buoyant convection. Although the role of Marangoni convection has been discussed in previous studies, the influence of gravity was hidden in the equations, and its importance has not been taken into account. Nevertheless, recognizing its impact provides valuable insights into the emerging instability and its underlying mechanisms. Taking into account all contributions, we have identified three regimes of convection driven by absorption.

In the first regime, convection is primarily driven by solute and thermal Marangoni stresses, which are nearly equal and act in opposite directions. However, thermal convection temporarily dominates, resulting in a flow directed towards the center. This unexpected direction was also experimentally observed[24]. Due to the opposite direction of Marangoni stresses, convection practically fades out by the end of the regime. However, the formation of inhomogeneous density in the horizontal direction gives rise to buoyancy convection.

The second regime is characterized by significant changes in fluid velocity, temperature distribution, and mass fraction. The buoyancy flow ascends to the interface from below, intensified by Marangoni convection, which occurs at the contact points of vortices with different directions. This leads to an increase in interfacial velocity by three orders of magnitude, a rupture of the boundary layer of the mass fraction and the involvement of the entire interface in motion. The lateral confinement leads to the fragmentation of the strong, elongated main roll into several smaller ones, each with an aspect ratio close to unity. Flow on the interface becomes multidirectional and loses energy. This creates an opportunity for the formation of small-scale Marangoni-driven flows.

The third regime is characterized by the formation of plumes, and establishing both temporal and spatial periodicity in the system. Small-scale Marangoni-driven flows, in turn, lead to the formation of 'lens-like' cells with lower mass fraction and density. Initially, these cells move left and right within the subsurface layer, but they later transform into almost stable plumes. As time progresses, the coupling between solutal, thermal, and buoyant convection exhibits competing and cooperative effects, resulting in the parallel existence of two types of patterns in different regions of space. These patterns, fueled by absorption, can be seen in space-time maps of mass fraction and velocity. The central part is occupied by vertical bands associated with plumes, which exhibit minimal changes over time, while a periodic structure near the wall becomes established with an almost constant period. We showed that this behavior can be characterized as a relaxation-oscillation mode of instability. The time evolution of the absorbed mass flux clearly exhibits the absorption-limited nature of the instability, illustrating the gradual loss of energy within the bands over time.

ACKNOWLEDGMENTS

The work is supported Elkartek program (KK-2023/00041-MMASINT) and Research Group Program (IT1505-22) of the Basque Government, and Grant PID2021-124232OB-I00 (Treated) funded by MCIN/AEI/10.13039/501100011033 and by ERDF "A way of making Europe"

CONFLICT OF INTEREST

The authors have no conflicts to disclose

AUTHOR CONTRIBUTION

P.F.A.: Data Curation, Formal Analysis, Software and Writing/Original Draft Preparation; M.M.A.: Data Curation, In-

vestigation and Visualization; A.N: Methodology, Validation and Writing/Reviewing and Editing; MM.B: Funding Acquisition, Validation and Writing-Review and Editing; VS: Funding Acquisition, Conceptualization, Supervision and Writing/Review and Editing.

DATA AVAILABILITY STATEMENT

The data that support the findings of this study are available from the corresponding author upon reasonable request.

[1]J. D. Killion and S. Garimella, "Gravity-driven flow of liquid films and droplets in horizontal tube banks," Int. J. Refrig. **26**, 516–526 (2003).
[2]C. Amaris, M. Valles, and M. Bourouis, "Vapour absorption enhancement using passive techniques for absorption cooling/heating technologies: A review," Applied Energy **231**, 826–853 (2018).
[3]S. Sehgal, J. L. Alvarado, I. G. Hassan, and S. T. Kadam, "A comprehensive review of recent developments in falling-film, spray, bubble and microchannel absorbers for absorption systems," Renewable and Sustainable Energy Reviews **142**, 110807 (2021).
[4]N. I. Grigoeva and V. E. Nakoryakov, "Exact solution of combined heat- and mass-transfer problem during film absorption," J. Eng. Physics **33**, 1349–1353 (1977).
[5]K. Schwarzenberger, T. Köllner, H. Linde, T. Boeck, S. Odenbach, and K. Eckert, "Pattern formation and mass transfer under stationary solutal marangoni instability," Adv. Colloid Interface Sci. **206**, 344–371 (2014).
[6]S. Shin, I. Jacobi, and H. A. Stone, "Bénard-marangoni instability driven by moisture absorption," Europhysics Letters **113**, 24002 (2016).
[7]D.-H. Rie and T. Kashiwagi, "Experimental study of steam absorption enhancement in accordance with interfacial turbulence into aqueous solution of libr : The influence of a noncondensable gas," JSME Int. J. Ser. 2, Fluids engineering, heat transfer, power, combustion, thermophysical properties **34**, 502–508 (1991).
[8]H. Daiguji, E. Hihara, and T. Saito, "Mechanism of absorption enhancement by surfactant," Int. J. Heat and Mass Transfer **40**, 1743–1752 (1997).
[9]J. S. Kim, H. Lee, and S. I. Yu, "Absorption of water vapour into lithium bromide-based solutions with additives using a simple stagnant pool absorber," Int. J. Refrig. **22**, 188–193 (1999).
[10]S. B. Park and H. Lee, "Heat and mass transfer of the new libr-based working fluids for absorption heat pump," Ind. Eng. Chem. Res. **41**, 1378–1385 (2002).
[11]V. E. Nakoryakov, N. I. Grigoryeva, N. S. Bufetov, and R. A. Dekhtyar, "Heat and mass transfer intensification at steam absorption by surfactant additives," Int. J. Heat Mass Transf. **51**, 5175–5181 (2008).
[12]S. Kulankara and K. E. Herold, "Theory of heat/mass transfer additives in absorption chillers," HVAC and R Research **6**, 369–380 (2000).
[13]N. S. Bufetov and R. A. Dekhtyar, "Investigation of transient regimes with steam absorption by water solution of lithium bromide," Thermophysics and Aeromechanics **28**, 125–136 (2021).
[14]P. F. de Arroiabe, A. Martinez-Urrutia, X. Peña, M. Martinez-Agirre, and M. M. Bou-Ali, "On the thermodiffusion effect in vertical plate heat exchangers," Eur. Phys. J. E **42**, 1–10 (2019).
[15]Y. Gaponenko, V. Yasnou, A. Mialdun, A. Nepomnyashchy, and V. Shevtsova, "Effect of the supporting disks shape on nonlinear flow dynamics in a liquid bridge," Phys. Fluids **33**, 042111 (2021).
[16]D. E. Melnikov, D. O. Pushkin, and V. M. Shevtsova, "Synchronization of finite-size particles by a traveling wave in a cylindrical flow," Phys. Fluids **25**, 092108 (2013).
[17]Y. Gaponenko, T. Yano, K. Nishino, S. Matsumoto, and V. Shevtsova, "Pattern selection for convective flow in a liquid bridge subjected to remote thermal action," Phys. Fluids **34**, 092102 (2022).
[18]M. Hozawa, M. Inoue, J. Sato, T. Tsukada, and N. Imaishi, "Marangoni convection during steam absorption into aqueous libr solution with surfactant," J. Chem. Eng. Jpn. **24**, 209–214 (1991).
[19]D.-H. Rie and T. Kashiwagi, "Numerical analysis of heat and mass transfer enhancement process accompanying interfacial disturbance in water vapor absorption," JSME Int. J. Ser B **36**, 636–643 (1993).
[20]J. Castro, L. Leal, C. D. Pérez-Segarra, and P. Pozo, "Numerical study of the enhancement produced in absorption processes using surfactants," Int. J. Heat Mass Transf. **47**, 3463–3476 (2004).
[21]A. B. Mikishev and A. A. Nepomnyashchy, "Instabilities in evaporating liquid layer with insoluble surfactant," Phys. Fluids **25**, 054109 (2013).
[22]B. Seta, A. Errarte, I. I. Ryzhkov, M. M. Bou-Ali, and V. Shevtsova, "Oscillatory instability caused by the interplay of Soret effect and cross-diffusion," Phys. Fluids **35**, 021702 (2023).
[23]Pranowo, D. A. Makarim, A. Suami, A. T. Wijayanta, N. Kobayashi, and Y. Itaya, "Marangoni convection within thermosolute and absorptive aqueous libr solution," Int. J. Heat Mass Transf. **188**, 122621 (2022).
[24]N. Bufetov, R. Dekhtyar, and V. Ovchinnikov, "An experimental investigation of thermocapillary convection in solution of lithium bromide with non-isothermal absorption," Vestnik of MSTU, in russian **19**, 673–679 (2016).
[25]N. Grigoreva and V. Nakoryakov, "Exact solution of combined heat- and mass transfer problem during film absorptions," J. Engineering Physics **33(5)**, 1349–1353 (1997).
[26]G. Grossman, "Simultaneous heat and mass transfer in film absorption under laminar flow," Int. J. Heat Mass Transfer **26**, 357–371 (1983).
[27]V. Nakoryakov and N. Grigoreva, "Nonisothermal absorption in thermotransformers," J. Engineering Thermophysics **19(4)**, 196–271 (2010).
[28]E. Hofmann and H. C. Kuhlmann, "On the optimum mass transfer of flat absorbing falling films," Int. J. Heat Mass Transf. **55**, 7686–7697 (2012).
[29]M. Wanschura, V. M. Shevtsova, H. C. Kuhlmann, and H. J. Rath, "Convective instability mechanisms in thermocapillary liquid bridges," Phys. Fluid **7**, 912–925 (1995).
[30]M. Lappa, *Fluids, Materials and Microgravity* (Elsevier, 2004).
[31]K. Schwarzenberger, S. Aland, H. Domnick, S. Odenbach, and K. Eckert, "Relaxation oscillations of solutal marangoni convection at curved interfaces," Colloids Surf. A Physicochem. Eng. Asp. **481**, 633–643 (2015).